

**LA-UR-21-20234**

Accepted Manuscript

# **Atomistic and cluster dynamics modeling of fission gas (Xe) diffusivity in TRISO fuel kernels**

Liu, Xiang-Yang

Matthews, Christopher

Jiang, Wen

Cooper, Michael William Donald

Hales, J. D.

Andersson, Anders David Ragnar

Provided by the author(s) and the Los Alamos National Laboratory (2022-01-24).

**To be published in:** Journal of Nuclear Materials

**DOI to publisher's version:** 10.1016/j.jnucmat.2022.153539

**Permalink to record:**

<http://permalink.lanl.gov/object/view?what=info:lanl-repo/lareport/LA-UR-21-20234>



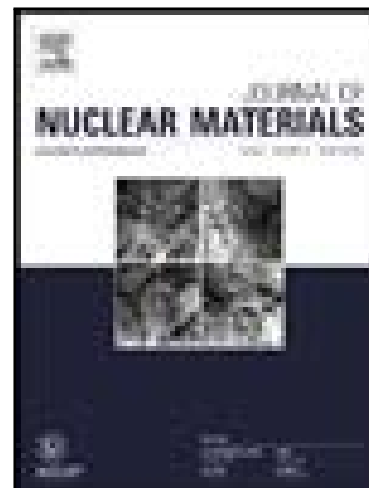
Los Alamos National Laboratory, an affirmative action/equal opportunity employer, is operated by Triad National Security, LLC for the National Nuclear Security Administration of U.S. Department of Energy under contract 89233218CNA000001. By approving this article, the publisher recognizes that the U.S. Government retains nonexclusive, royalty-free license to publish or reproduce the published form of this contribution, or to allow others to do so, for U.S. Government purposes. Los Alamos National Laboratory requests that the publisher identify this article as work performed under the auspices of the U.S. Department of Energy. Los Alamos National Laboratory strongly supports academic freedom and a researcher's right to publish; as an institution, however, the Laboratory does not endorse the viewpoint of a publication or guarantee its technical correctness.

## Journal Pre-proof

Atomistic and cluster dynamics modeling of fission gas (Xe) diffusivity in TRISO fuel kernels

X.-Y. Liu, C. Matthews, W. Jiang, M.W.D. Cooper, J.D. Hales, D.A. Andersson

PII: S0022-3115(22)00035-6  
DOI: <https://doi.org/10.1016/j.jnucmat.2022.153539>  
Reference: NUMA 153539



To appear in: *Journal of Nuclear Materials*

Received date: 22 January 2021  
Revised date: 7 January 2022  
Accepted date: 13 January 2022

Please cite this article as: X.-Y. Liu, C. Matthews, W. Jiang, M.W.D. Cooper, J.D. Hales, D.A. Andersson, Atomistic and cluster dynamics modeling of fission gas (Xe) diffusivity in TRISO fuel kernels, *Journal of Nuclear Materials* (2022), doi: <https://doi.org/10.1016/j.jnucmat.2022.153539>

This is a PDF file of an article that has undergone enhancements after acceptance, such as the addition of a cover page and metadata, and formatting for readability, but it is not yet the definitive version of record. This version will undergo additional copyediting, typesetting and review before it is published in its final form, but we are providing this version to give early visibility of the article. Please note that, during the production process, errors may be discovered which could affect the content, and all legal disclaimers that apply to the journal pertain.

© 2022 Published by Elsevier B.V.

# Atomistic and cluster dynamics modeling of fission gas (Xe) diffusivity in TRISO fuel kernels

X.-Y. Liu<sup>a</sup>, C. Matthews<sup>a</sup>, W. Jiang<sup>b</sup>, M. W. D. Cooper<sup>a</sup>, J. D. Hales<sup>b</sup>, D. A. Andersson<sup>a</sup>

<sup>a</sup>Materials Science and Technology Division, Los Alamos National Laboratory, Los Alamos, NM 87545, USA

<sup>b</sup>Computational Mechanics and Materials, Idaho National Laboratory, Idaho Falls, ID 83415, USA

---

## Abstract

TRISO fuel particles are candidates for use in next generation reactors including gas reactors, fluoride salt-cooled high temperature reactors, and micro-reactors. The UCO fuel kernel consists of a uranium dioxide ( $\text{UO}_2$ ) and uranium carbide mixture. The addition of  $\text{UC}_2$  helps suppress the formation of carbon monoxide gas, which led to failures during initial TRISO development. The addition of uranium carbide alters the chemistry of the  $\text{UO}_2$  pellet, which is known to influence performance parameters such as fission gas diffusivity, although the impact has not been quantified and no models exist that take the change in chemistry into account. Therefore, better understanding and more accurate models of the impact of chemistry on fuel performance are of high priority. In this paper, a first-principles density functional theory (DFT) and empirical potential based multi-scale study has been carried out to model the diffusivity of fission gas xenon (Xe) in UCO TRISO fuel kernels. The focus is on the  $\text{UO}_2$  component in the UCO fuel kernels, as that represents the largest volume fraction of the fuel kernels. The study relies on DFT and empirical potential calculations to determine Xe and point defect properties, which are then used in thermodynamic and kinetic models to predict diffusion for intrinsic conditions. In addition, the information is utilized in cluster dynamics simulations using the Centipede code to estimate the impact of irradiation on defect transport. The presence of  $\text{UC}_2$  or  $\text{UC}_{2-x}$  in the UCO fuel kernels is shown to have a substantial impact on the  $\text{UO}_2$  non-stoichiometry by inducing oxygen vacancies and driving  $\text{UO}_2$  sub-stoichiometric, which causes much slower Xe diffusion in UCO compared to light water reactor  $\text{UO}_2$  fuel. The application of this model in fuel performance simulations using the Bison code is also demonstrated.

---

## 1. Introduction

Tristructural isotropic coated (TRISO) fuel particles have historically been used in high-temperature gas-cooled reactors (HTGR), and consist of a uranium bearing kernel in the form of either  $\text{UO}_2$  or UCO, a porous carbon buffer, an inner pyrolytic carbon (IPyC) layer, a silicon carbide layer, and an outer pyrolytic carbon (OPyC) layer [1, 2].  $\text{UO}_2$  was initially utilized as the fuel form, but fuel oxidation during burnup caused reaction with the porous carbon buffer and formation of CO gas, which led to safety issues [1]. UCO fuel kernels are made from a mixture of  $\text{UO}_2$  and uranium carbide, and are considered to be more accident tolerant for use in next generation reactors. This is because the reducing nature of uranium carbides prevents formation of CO gas, as will also be further discussed in this paper based on first-principles den-

sity functional theory (DFT) calculations. More recently, TRISO fuels are also being considered for usage in fluoride salt-cooled high temperature reactors (FHR) [3], as well as in micro-reactor technology [4].

Given the importance of TRISO fuels for advanced reactor concepts that are actively pursued by industry, better understanding and more accurate performance models of the TRISO fuel kernels are high priorities [5]. This includes the diffusion parameters governing transport of the fission gas xenon (Xe) and fission products such as silver (Ag) and palladium (Pd), which are important input parameters to the fission gas and product release models used in fuel performance codes. The current state-of-the-art models in fuel performance codes such as PARFUME [6] still use models based on the Xe release data obtained from light water reac-

tor (LWR)  $\text{UO}_2$  fuel, which is nearly stoichiometric or slightly hyper-stoichiometric. However, in actual UCO fuel kernels, the fission gas release rate is expected to be different, as a consequence of the more reducing conditions in UCO compared to LWR  $\text{UO}_2$  fuel. The Xe diffusion coefficient is known to be very sensitive to the fuel non-stoichiometry [7].

Experimental measurements of fission gas release in UCO fuel kernels have been very limited. In the early days of the HTGR endeavor, which was active until 1977, the experimental efforts to measure diffusivity data were focused on pure  $\text{UO}_2$ ,  $\text{ThO}_2$ ,  $\text{UC}_2$ , or UN. These measurements were critically reviewed by Matzke [8]. While UCO fuel kernels had been conceived and manufactured starting in the early 80s, most experimental work focused on technology comparison, i.e., to determine what is the minimum fraction of required uranium carbides in UCO fuel kernels to avoid formation of CO gas [9–11], with much less emphasis on the fission gas release rates.

In the present study, lower length scale modeling and simulations of fission gas – here focusing on Xe to estimate the behavior of all fission gases – diffusion in UCO TRISO fuel kernels have been carried out. This work extends earlier investigations of fission gas diffusion in  $\text{UO}_2$  for light water reactors under both intrinsic conditions and under irradiation [12–15]. The approach relies on DFT and empirical potential calculations to determine Xe and point defect properties, which are then used in thermodynamic and kinetic models to predict diffusion for intrinsic conditions. In addition, the information is utilized in cluster dynamics simulations for the irradiation response. The result is a model for fission gas diffusivity as a function of temperature and fission rate in UCO fuel kernels that can be used for simulations of fission gas retention/release in fuel performance codes, such as Bison [16–18]. The application of this model in Bison simulations is also demonstrated. The new Xe diffusion model is the first Xe diffusion model specifically developed for UCO fuel kernels and, as will be shown, the previous assumption that diffusion is similar to that in LWR  $\text{UO}_2$  fuels leads to rather significant over-prediction of fission gas diffusion and release. In order to develop the Xe diffusion model for UCO fuels, a number of supporting analysis steps were first carried out. They include the following,

- DFT calculations of phase stability of the constituent  $\text{UO}_2$ ,  $\text{UC}_x$  and  $\text{U}(\text{O,C})_2$  solution

phases in UCO fuel kernels;

- DFT and empirical potential calculations, and thermodynamic analysis of non-stoichiometric  $\text{UO}_2$  in UCO fuel kernels;
- DFT calculations of fission gas migration energies in the  $\text{UO}_2$  phase of UCO fuel kernels;
- Cluster dynamics simulations of point defects and cluster concentrations in irradiated UCO fuel kernels using the Centipede code [14, 15], which enables calculation of diffusion coefficients under irradiation conditions.

Although the work is heavily based on DFT and empirical potential calculations of defect formation and migration energies and entropies, without a good understanding of the thermo-chemistry in the UCO system it is not possible to predict the relevant diffusivities, which motivates starting off by investigating the foundational thermo-chemistry of UCO TRISO fuel kernels. After accounting for the UCO thermochemistry, the final step of the study involves using the Centipede cluster dynamics code [14, 15] with parameters obtained from DFT and empirical potential calculations to predict the fission gas (Xe) diffusivity under both thermal equilibrium and irradiation conditions in UCO fuel kernels. The study is focused on the  $\text{UO}_2$  component, since that is the dominant phase in the UCO fuel kernels.

The structure of this paper is as follows: After introduction of the methods used, the results of the steps outlined above are each separately reported, followed by the implementation of the new diffusivity model into Bison simulations, and finally a summary is presented.

## 2. Methods

### 2.1. DFT+ $U$ calculations

DFT+ $U$  calculations are used for defect energies, defect volumes and migration barriers. The calculations are performed with the Vienna ab initio simulation package (VASP) [19–21] using the projector-augmented-wave (PAW) method [22, 23]. The GGA-PBE exchange correlation potential is used with Hubbard  $U$  (onsite Coulomb parameter) and  $J$  (onsite exchange parameter) terms included for the uranium  $5f$  orbitals in order to capture the effects of strong correlations. The rotational invariant functional form due to Liechtenstein et

al. [24] is employed. To simplify the calculation of defect properties, spin-orbit coupling and non-collinear magnetism are ignored. The collinear  $1\mathbf{k}$  anti-ferromagnetic (AFM) ordering of uranium (U) spins is considered, which is slightly different from the  $3\mathbf{k}$  AFM ordering observed in experiments at low temperatures but it is known to be a reasonable approximation for the high-temperature paramagnetic state of interest to nuclear fuel applications. The  $U$  and  $J$  parameters are set to 4.5 and 0.51 eV, respectively, as determined from analysis of X-ray photoemission spectra [25]. We apply this choice of parameters to both  $\text{UO}_2$  and  $\text{UC}_2$ , as was practiced in an earlier study [26].

For defect calculations, a  $2\times 2\times 2$  (96 atoms) supercell expansion of the  $\text{UO}_2$  fluorite unit cell and a  $2\times 2\times 2$  (48 atoms) supercell expansion of the  $\text{UC}_2$  tetragonal unit cell are used.  $2\times 2\times 2$  ( $\text{UO}_2$ ) and  $4\times 4\times 2$  ( $\text{UC}_2$ ) Monkhorst-Pack k-point meshes and a plane-wave cutoff energy of 500 eV are used for the defect calculations. The force convergence criteria is 0.05 eV/Å for ionic relaxations. The migration barriers are calculated using the Nudged Elastic Band (NEB) method with the improved climbing image algorithm [27].

DFT+ $U$  calculations for  $\text{UO}_2$  are known to yield metastable electronic solutions [28]. In order to avoid this problem all simulations are performed without any assumptions regarding the crystal symmetry, this is done through introduction of small distortions. At least one of the following approaches, the orbital matrix occupation control methodology developed by Dorado et al. [28] or the  $U$  ramping method due to Meredig et al [29] have been applied to avoid metastable solutions. The VASP calculations for the  $\text{UO}_2$  supercell structures use the ISYM=2 tag, even though the structural relaxations assume no symmetry through introduction of small distortions. It has been shown that this setting gives results consistent with  $\text{UO}_2$  without Jahn-Teller distortions [13]. If symmetries are completely turned off (ISYM=0) then the full Jahn-Teller solution is obtained. The charged defect calculations are carried out by adding or removing electrons from the supercells and the energy corrections due to the charged supercells employ the procedure suggested by Taylor and Bruneval [30]. The corrected total energy is expressed as,

$$E(\epsilon_F) = E_0 + q\epsilon_F + \text{correction term}, \quad (1)$$

where  $E_0$  is the total energy from the charged supercell calculations (before correction),  $q$  is the to-

tal charge of the supercell,  $\epsilon_F$  is the Fermi level starting from the top of the valence band, and the correction term is the associated Coulomb correction and potential shift (for which we apply the procedure suggested by Taylor and Bruneval [30]). This treatment is similar to charged defect calculations in actinide oxides from other works, for example, charge effects for  $\text{UO}_2$  clusters [13], iodine charge effect [31], and Cr doping effects in  $\text{UO}_2$  [32]. The Fermi level can go from zero to the bandgap of  $\text{UO}_2$ , for which the experimental value of 2.1 eV [33] is used.

## 2.2. Empirical potential calculations

Vibrational defect entropies are calculated from the normal mode phonon frequencies, an approach similar to our earlier works [12, 34–36]. The phonon frequencies are calculated using GULP [37] employing the many-body potential developed by Cooper, Rushton and Grimes (CRG) for  $\text{UO}_2$  [38]. At temperatures higher than the Debye temperature, the entropy of crystalline solids can be approximated as

$$S = -k_B \sum_{n=1}^{3N-3} \ln \left( \frac{h\nu_n}{k_B T} \right) + (3N-3) k_B, \quad (2)$$

where  $N$  is the number of atoms in the crystal,  $k_B$  is the Boltzmann constant,  $T$  is the temperature, and  $\nu_n$  is the normal vibrational frequency of the crystal. There are three modes that are zero for every supercell, corresponding to translational modes, which are neglected. In the harmonic approximation used here, the normal mode vibrational frequencies are calculated by diagonalizing the dynamical force matrix of the system at a constant volume.

The entropy relevant for nuclear fuels is at constant pressure ( $S_P$ ), which is calculated from the constant volume entropies according to

$$S_P = S_V + \beta V_{rel}, \quad (3)$$

where  $\beta$  is  $\left(\frac{\partial S}{\partial V}\right)_T$ ,  $V$  is the volume.  $V_{rel}$  is the volume change at zero pressure for the crystal with defects. For  $\text{UO}_2$ ,  $\beta$  is computed to be  $0.447 k_B/\text{\AA}^3$ . The defect volumes are obtained from DFT calculations. At high temperatures, anharmonic effects contribute to the defect formation entropies and energies. This contribution can be included through the quasi-harmonic approximation, which calculates energies and phonons at several different

volumes to account for the effect of thermal expansion. The neglect of anharmonicity in our calculations could affect the accuracy of the results at high temperatures.

### 2.3. Defect model

Point defect concentrations under thermal equilibrium conditions may be computed using a point defect model. The particular approach applied here is described in detail in earlier publications [35, 39]. Within this model, the concentration of a given defect  $i$  is determined by its associated Gibbs free energy,

$$c_i = m_i \exp(-\Delta G_f^i/k_B T), \quad (4)$$

where  $m_i$  is the multiplicity of the defect. The Gibbs free energy is,

$$\Delta G_f^i = \Delta E - T\Delta S + q_i\mu_e + \sum_{\alpha} n_{\alpha}\mu_{\alpha}, \quad (5)$$

where  $\mu_e$  is the electron potential of the system,  $q_i$  is the charge of the defect, and the chemical potential of species  $\alpha$  is given by  $\mu_{\alpha}$ .  $\Delta E$  and  $\Delta S$  are determined by atomic scale simulations according to,

$$\Delta E = E_{defect} - E_{perfect}, \quad (6)$$

$$\Delta S = S_{defect} - S_{perfect}, \quad (7)$$

where  $E$  and  $S$  denote DFT supercell energies and empirical potential supercell entropies, respectively. The oxygen and uranium chemical potentials are defined by<sup>1</sup>:

$$\mu_O = -5.23975 - \frac{0.002488T}{2.0} + \frac{k_B T \log(P_{O_2}/P_{O_2}^0)}{2.0} \quad (\text{in eV}) \quad (8)$$

$$\mu_U = \mu_{UO_2} - 2\mu_O, \quad (9)$$

where  $T$  is temperature,  $P_{O_2}$  is the oxygen partial pressure of the system,  $P_{O_2}^0$  is the reference standard atmosphere pressure, and  $\mu_{UO_2}$  equals to the Gibbs free energy of  $UO_2$  per formula unit.

<sup>1</sup>The second term without the factor  $T$  in Eq. (8) corresponds to the entropy contribution in the oxygen chemical potential, which is set equal to  $\frac{1}{2}$  of the standard entropy value of an oxygen molecule at 900 K, 240 J/K.mol (28.87  $k_B$ ) [40]. See also Table 3. In reality, this term depends on temperature, but the current approximation is sufficient for the present analysis and consistent with previous treatments [14, 15, 32, 41]

The total charge concentration in the system is defined by  $\sum_i q_i c_i$ . All defects have their formal charges (e.g., oxygen vacancy has a formal charge of  $+2|e|$ ). The concentrations of all charged defects in the system vary as a function of  $\mu_e$  due to its influence on the formation energies.  $\mu_e$  is adjusted until the criteria for charge neutrality,  $\sum_i q_i c_i = 0$ , is achieved and the final defect concentrations are determined (for a given  $T$  and  $P_{O_2}$ ).

### 2.4. Centipede cluster dynamics simulations

The free energy cluster dynamics (FECD) framework was developed by Matthews et al. and is implemented in the Centipede code [14, 15]. The framework has been applied to the concentration and diffusivity of defects to describe self-diffusion [14] and Xe diffusion [15, 41] in  $UO_2$  under irradiation. The results demonstrate the successful application of this framework to capture the transition between irradiation enhanced diffusion and thermal equilibrium diffusion for uranium self- and Xe diffusion. For this work, we have extended the Xe diffusion model [15], which was parameterized using DFT data published by Perriot et al. [13]. A detailed description of the framework can be found elsewhere [14, 15], however a brief description of the method will be given here.

The concentrations of defects in the  $UO_2$  system under irradiation are calculated by solving a set of ordinary differential equations (ODEs) that capture a number of phenomena including: production of Frenkel pairs through irradiation, mutual recombination of Frenkel pairs, interaction with sinks, and clustering of point defects. For the concentration,  $c_d$ , of a given defect,  $d$ , the ODE can be expressed as:

$$\frac{dc_d}{dt} = \dot{\beta}_d + \sum_C \dot{R}_{d,C}(c_d, c_C, T, G) - \sum_s \dot{S}_{d,s}(c_d, c_s, T, G) \quad (10)$$

where  $\dot{\beta}_d$  describes the source rate of defects through irradiation.  $\dot{R}_{d,C}$  and  $\dot{S}_{d,s}$  are the cluster and sink rates, which depend on the defect concentration ( $c_d$ ), the concentration of a given cluster ( $c_C$ ), the sink concentration ( $c_s$ ), the temperature  $T$ , and the free energy of the system  $G$ . Centipede simulations find the steady-state solution to this coupled set of ODEs, such that  $\frac{dc_d}{dt} \leq \mathcal{R}$  for all defects, where  $\mathcal{R}$  is the convergence criteria. The re-

action rate,  $\dot{R}_d$ , for a given reaction,  $A+B \rightarrow Y+Z$ , can be expressed as:

$$\dot{R}_d = \begin{cases} \frac{k_i^2}{\Omega} D \left[ x_A x_B - x_Y x_Z \exp\left(\frac{\Delta G^0}{k_B T}\right) \right], & (\text{if } \Delta G^0 < 0) \\ \frac{k_i^2}{\Omega} D \left[ x_A x_B \exp\left(-\frac{\Delta G^0}{k_B T}\right) - x_Y x_Z \right], & (\text{otherwise}) \end{cases} \quad (11)$$

where  $k_B$  is the Boltzmann constant,  $\Omega$  is the atomic volume,  $k_i$  is a reaction rate constant, and  $D = D_A + D_B$  is the sum of the diffusivities of the reactants.  $x_A$  and  $x_B$  are the atom fractions of the reactants and  $x_Y$  and  $x_Z$  are the atom fractions of the products.  $\Delta G^0$  is the binding energy of the reaction. A detailed explanation of the application of Eqs. (10) and (11) to Xe in  $\text{UO}_2$  is given in Refs. [14, 15]. Note that the switching criteria in Eq. (11) is based on the change in the concentration-independent defect energies of the reaction,  $\Delta G^0$ , and not the driving force,  $f$ , which was mistakenly utilized in previous work. It is also worth noting that the modeling choices adapted in [14] differ from traditional cluster dynamics techniques through the modification of the reaction rate when  $\Delta G^0 < 0$ . This is motivated by evidence from previous theoretical studies [42] and atomistic simulations [43] that show the activation barrier is not completely independent on the net energy of the reaction. Both models (Eq. (11) with and without the conditional term) have been tested and shown to have minimal impact on the steady-state simulations performed here, and those from previous works [14, 15, 41]. Xe diffusion in  $\text{UO}_{2-x}$ , which is the composition range of interest in UCO fuel kernels, may involve a few mechanisms related to oxygen vacancy defects that were not included in the previous analysis, since they were not expected to be important in the  $\text{UO}_{2+x}$  range relevant for LWR fuel. The new mechanisms and calculation of the corresponding model parameters will be discussed in Section 5.

### 2.5. Bison simulations

Given the fission gas diffusivity model calculated by Centipede, the fission gas release (FGR) from the UCO fuel kernel can be calculated using Bison. Here, FGR represents the amount of fission gas that is released by the UCO kernel into the void volume

of the TRISO particle (kernel and buffer porosities and buffer-IPyC gap).

The FGR is calculated from both direct recoil release and diffusive release as:

$$FGR = (RF_{recoil} + [1.0 - RF_{recoil}]RF_{Booth})FGP \quad (12)$$

where  $RF_{recoil}$  and  $RF_{Booth}$  are the release fractions of fission gas by direct recoil and diffusion, respectively, and  $FGP$  is the amount of fission gas produced in the kernel.

#### 2.5.1. Direct recoil

Direct kinetic release of fission gases from the kernel to the buffer is accounted for by geometrical considerations and fission fragment ranges derived from compiled experimental data [44].

The fission gas mixture is essentially composed of krypton (Kr) and Xe, with relative fractions of 18.5 and 81.5% [6]. Hence, the recoil fraction is given by:

$$RF_{recoil} = 0.185RF_{recoil,Kr} + 0.815RF_{recoil,Xe} \quad (13)$$

where  $RF_{recoil,Kr}$  and  $RF_{recoil,Xe}$  are the respective release fractions of Kr and Xe due to recoil.

#### 2.5.2. Booth model

Diffusive release through kernel grains to the grain boundaries and subsequent transport through the interconnected porosity is estimated by the Booth equivalent sphere diffusion model [45].

The Booth release fraction is given by:

$$RF_{Booth} = 1.0 - \frac{6.0r_{grain}^2}{Dt} \sum_{n=1}^{\infty} \frac{1.0 - \exp\left(\frac{-n^2\pi^2 D_{eff}t}{r_{grain}^2}\right)}{n^4\pi^4} \quad (14)$$

where  $r_{grain}$  is the radius of the diffusing sphere (i.e., the average grain radius),  $D_{eff}$  is the diffusivity of the fission gas in the grain, and  $t$  is the diffusion time.

The effective diffusivity is described as [46]

$$D_{eff} = D \frac{b}{b+g} \quad (15)$$

where  $g$  is the trapping rate,  $b$  is the resolution rate and  $D$  is the unperturbed diffusivity.

The trapping [47] and resolution [48] parameters are given by:

$$g = 4\pi RND, \quad (16)$$

and

$$b = 3.03f'''\pi l_f(R + Z_0), \quad (17)$$

where  $l_f = 6 \times 10^{-6}$  m is the length of a fission fragment track,  $Z_0 = 10^{-9}$  m is the radius of influence of a fission fragment, and  $f'''$  is the fission rate density. The bubble radius and bubble density,  $R$  and  $N$  respectively, are given as [48]

$$R = 5 \times 10^{-10}(1 + 106 \cdot \exp(-8691.6/T)), \quad (18)$$

and

$$N = \frac{1.52 \times 10^{27}}{T} - 3.3 \times 10^{23}. \quad (19)$$

The unperturbed Xe diffusivity model utilizes the total diffusion coefficient,  $D$ , formulated for  $\text{UO}_2$  fuel from a recent work by Matthews et al. [15] as:

$$D = \sum_{i=1}^3 D_i = D_1 + D_2 + D_3 \quad (20)$$

where  $D_1$ ,  $D_2$ , and  $D_3$  are the diffusion coefficients of the mechanisms controlling diffusion at different temperature ranges. The parameters detailed below are the currently existing ones, also termed as “the  $\text{UO}_2$  model”, before incorporating the lower length scale Xe diffusivity model (developed for UCO fuels) into Bison.

$$D_1 = \frac{2.216 \times 10^{-7} \exp(-\frac{37832}{T})}{1 + 29.0 \exp(-\frac{24353}{T})}, \quad (21)$$

$$D_2 = 2.821 \times 10^{-22} \exp(-\frac{23209}{T}) \sqrt{f'''} (\text{m}^2/\text{s}), \quad (22)$$

$$D_3 = 8.5 \times 10^{-40} f''' (\text{m}^2/\text{s}), \quad (23)$$

where  $T$  is the temperature of the kernel in K;  $f'''$  is the fission rate density, which is used to create agreement with the revised experimental results reported, as [49] compared to [50].

### 2.5.3. Fission gas production

The amount of fission gas produced by the kernel,  $FGP$ , during a time interval  $\Delta t$ , is calculated as:

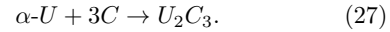
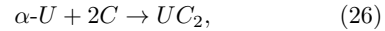
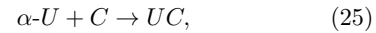
$$FGP = \frac{\Gamma_{FG} f''' V_k \Delta t}{N_a} \quad (24)$$

where  $\Gamma_{FG}$  is the combined fractional fission yield of Kr and Xe atoms per fission,  $V_k$  is the volume of the kernel, and  $N_a$  is Avogadro’s number.

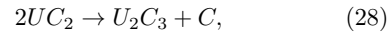
## 3. Thermo-chemistry and defect analysis

### 3.1. Uranium carbides in UCO fuel kernels

Understanding the thermo-chemistry of complex fuel materials such as UCO involves investigating the possibility of a solution phase versus a composite multi-phase microstructure, as well as the impact of the phase distribution on non-stoichiometry of the constituent phases. The importance of thermochemistry for nuclear fuel performance and fission gas release has been demonstrated for doped  $\text{UO}_2$  [32, 41], where the change in the oxygen chemical potential due to addition of  $\text{Cr}_2\text{O}_3$  shifts the non-stoichiometry of  $\text{UO}_{2+x}$  sufficiently to impact the irradiation enhanced Xe diffusivity significantly compared to the undoped case. As will be shown later, the impact of carbides on the oxygen potential, and by extension Xe diffusion, is even bigger. The thermo-chemistry of UCO fuel kernels depends on the uranium carbide phases present. Uranium carbide can exist in three forms in nature, UC,  $\text{UC}_2$ , and  $\text{U}_2\text{C}_3$  [51–53], and can form according to the following chemical reactions between carbon and metallic uranium ( $\alpha\text{-U}$ ),



In the uranium-carbon phase diagram, both  $\text{U}_2\text{C}_3$  and  $\text{UC}_2$  exist for C/U ratio of around 2, with  $\text{U}_2\text{C}_3$  suggested as the more stable phase below 1787 K [52]. It is reported [51] that  $\text{UC}_2$  can decompose into  $\text{U}_2\text{C}_3$  through the following reaction,



however, this reaction has very slow kinetics and, consequently, it is typically not considered [51]. From recent experimental characterizations, it is clear that  $\text{UO}_2$ ,  $\text{UC}_2$ , and UC co-exist in UCO kernels in TRISO fuels [54]. For carbides, the tetragonal phase ( $\alpha\text{-UC}_2$ ) of  $\text{UC}_2$  dominates [54]. While the possible existence of or transition to UC and  $\text{U}_2\text{C}_3$  is also worth further exploration, we have focused our modeling effort on understanding the thermo-chemistry of UCO fuel in terms of  $\text{UO}_2$  and  $\text{UC}_2$  mixtures. The phase mixture containing UC ( $\text{UO}_2$ , UC,  $\text{UC}_2$ ) [53] is not considered in our modeling work. Thus, our work will not cover phase regions involving UC compound in the phase diagram [53]. The main conclusions from this study

should extend to cases with other or additional carbides phases present, even though the Xe diffusivity is expected to change slightly as function of changes in oxygen partial pressure induced by other or additional carbides being present in the phase mixture.

### 3.2. $UO_2$ - $UC_2$ dilute heats of mixing

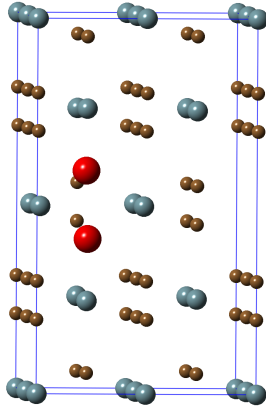


Figure 1: The lowest energy configuration with a pair of oxygen atoms in  $UC_2$ . Solid red spheres are oxygen atoms. Grey spheres are uranium atoms. Brown spheres are carbon atoms.

The ground state of  $UC_2$  ( $\alpha$ - $UC_2$ ) is an AFM, metallic tetragonal phase with space group  $I4/mmm$ , stable up to 2073 K [55]. The first step in the DFT+ $U$  study is to compute the dilute heats of mixing of the  $UO_2$  and  $UC_2$  phases. These are calculated as the energy cost for a C atom to replace an oxygen atom in  $UO_2$  (substitutional mixing) or an oxygen atom to replace a C atom in  $UC_2$  (substitutional mixing) with the parent phases as references. The effect of bonding environment on mixing is investigated by adding two oxygen impurity atoms close to each other in the  $UC_2$  host matrix phase. This gives us an indication of how well a single substitution atom works as a model for the solution thermodynamics. The choice of  $UC_2$  over  $UO_2$  for the impurity bonding study is based on a geometrically simpler bonding arrangement in this phase. The different geometrical arrangements of oxygen pairs in  $UC_2$  are calculated and the lowest energy configuration, as shown in Fig. 1, is selected for the reported dilute heats of mixing energies. The results are listed in Table 1. Due to the high positive heats of mixing values ( $> 2$  eV), we conclude that  $UO_2$  and  $UC_2$  are insoluble in each

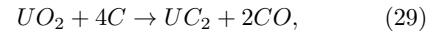
other, and should exist as separate crystal phases in the UCO fuel kernels. This agrees with experimental observations [56]. In addition, the ternary phase diagram of Ref. [53] also shows  $UO_2$  and  $UC_2$  do not significantly mix.

Table 1: The dilute heats of mixing of  $UC_2$  in  $UO_2$  and  $UO_2$  in  $UC_2$  from DFT+ $U$  calculations. All energies listed are per impurity atom.

	$UC_2$ in $UO_2$	$UO_2$ in $UC_2$
$\Delta H_m$ (eV)	2.91	2.51
$\Delta H_m$ (eV) (impurity pair)	-	2.66

### 3.3. UCO thermo-chemistry and oxygen vacancy defects in $UO_2$

After establishing that  $UO_2$  and  $UC_2$  exist as separate phases in UCO fuel kernels, calculations are performed to understand the role of  $UC_2$  on formation of CO gas and  $UO_2$  non-stoichiometry. In the early experimental measurements of high temperature phase equilibria in the carbon-oxygen-uranium system [57, 58], the so called ‘‘carbothermic’’ reduction involving the following chemical reactions,



were studied. From these experimental measurements, the thermodynamic functions were determined, i.e., the formation enthalpy ( $\Delta H$ ) and entropies ( $\Delta S$ ). These chemical reactions are the reactions to produce the UCO fuel kernel in the production stage. However, they are not the reactions that determine the UCO thermal equilibrium in the fuel kernel.

Table 2: DFT+ $U$  calculated reaction enthalpy in chemical reaction Eq. (31) and Eq. (32), in comparison with the calculated reaction enthalpy using thermodynamic functions. For the calculated reaction enthalpy using thermodynamic functions, Eq. (33) instead of Eq. (31) is used. The units are in eV. The reaction entropies using the the thermodynamic functions are also listed, with units in  $k_B$ .

Reactions	DFT + $U$ $\Delta H$	thermo. functions	
		$\Delta H$	$\Delta S$
Eq. (31) (eV)	-10.6	-10.3	-22.5
Eq. (32) (eV)	-6.4	-6.3	-0.45

Due to the effects of burn-up, the  $UO_2$  component in the UCO fuel kernel is expected to generate excess oxygen (oxygen interstitials in  $UO_2$ ) due

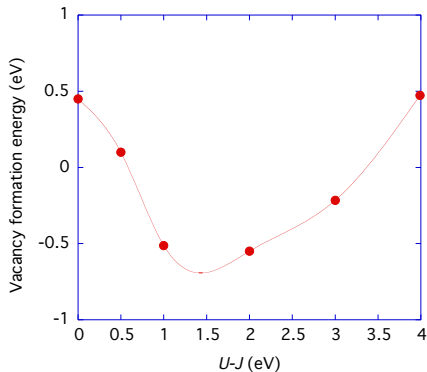
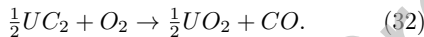
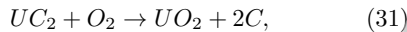


Figure 2: The carbon vacancy formation energy in  $UC_2$  computed from DFT+ $U$  for different on-site Hubbard term ( $U - J$ ) used in the DFT+ $U$  calculations.

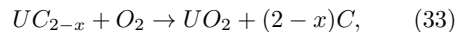
to the fissioning of U atoms. In UCO kernels, the excess oxygen may react with the carbide phase according to the following two chemical reactions,



We have performed DFT+ $U$  calculations for these two reactions. The results are listed in Table 2, in comparison with calculations using thermodynamic functions derived from experiments [52, 59]. In Table 2, since only the enthalpy differences are used, the temperature dependence of the enthalpy is not considered and we assume the temperature dependence to cancel. For the thermodynamic functions, the standard state values, or the experimental data at room temperature (298 K) are used. For the DFT data, 0 K values are used. Both chemical reactions are exothermic. In agreement with experiments, DFT calculations confirm that reaction Eq. (31) has much larger enthalpy reduction than reaction Eq. (32), therefore, carbon (in graphite form) is preferred over CO gas as a reaction product. The prevention of CO gas formation is the rationale for adding the carbide phase in the first place and effectively eliminates CO pressure in the UCO fuel kernels. Further consideration of reaction entropies does not change this trend. Including sufficient  $UC_2$  in the fuel serves the purpose of getting the excess oxygen produced by  $UO_2$  during fission reactions, thereby avoiding formation of CO while still taking advantage of the superior retention of fission products in  $UO_2$  [1]. The results

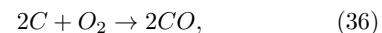
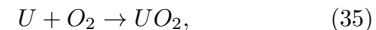
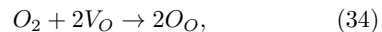
of our calculations are, consequently, in agreement with this intended purpose of the  $UC_2$  additions. For the rest of this paper, reaction Eq. (31) is assumed to determine the UCO thermal equilibrium in the fuel kernel.

The experimental phase diagram [52] indicates that  $UC_2$  may accommodate sub-stoichiometry,  $UC_{2-x}$ , with  $x$  typically equal to 0.1 ( $UC_{1.9}$ ). Eq. (31) then becomes,



which implies that the same mechanism to prevent CO formation is still valid. In order to test if the DFT+ $U$  calculations agree with the formation of sub-stoichiometry  $UC_{2-x}$ , the carbon vacancy formation energy in  $UC_2$  is calculated. As shown in Fig. 2, the carbon vacancy formation energy in  $UC_2$  is low (less than 0.5 eV), with actual values depending on the Hubbard term ( $U-J$ ) used in the DFT+ $U$  calculation<sup>2</sup>. The low value of the vacancy formation energy confirms the high-temperature experimental phase diagram, which also justifies the use of the thermodynamic functions of  $UC_{2-x}$  in our work, using Eq. (33) (based on the experimental measurements of a non-stoichiometric  $UC_2$ ).

The presence of  $UC_2$  or  $UC_{2-x}$  in the UCO fuel kernels is shown below to have a substantial impact on the  $UO_2$  non-stoichiometry by inducing oxygen vacancies and driving  $UO_2$  sub-stoichiometric. In thermodynamics, the Ellingham diagram is a useful tool showing the dependence of the compound stability on temperature, especially in metal oxide systems. It plots the Gibbs free energy of formation of metal oxides,  $\Delta G$ , as a function of temperature. The lower the position of a line in the Ellingham diagram, the greater is the stability of the metal oxide. In Fig. 3, the Ellingham diagram of four chemical reactions governing the equilibria in UCO fuels is plotted. Besides the chemical reaction in Eq. (33), the three other chemical reactions below are included,



in which  $V_O$  is the oxygen vacancy in  $UO_2$ . For reaction Eq. (34), two versions are provided: one

<sup>2</sup>The carbon chemical potential used for the carbon vacancy formation energy calculations in  $UC_2$  is solid carbon in its diamond form.

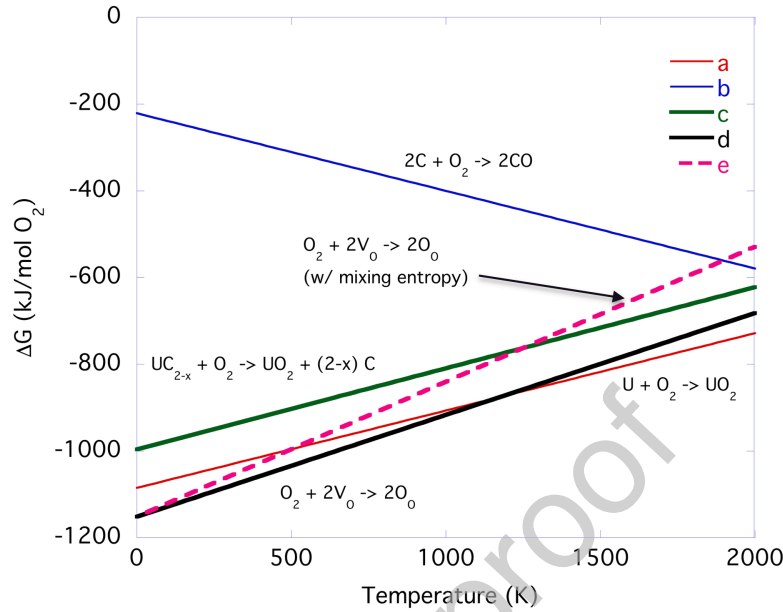


Figure 3: Ellingham diagram plot showing chemical reactions (a)  $U + O_2 \rightarrow UO_2$  (Eq. (35)), (b)  $2C + O_2 \rightarrow 2CO$  (Eq. (36)) (c)  $UC_{2-x} + O_2 \rightarrow UO_2 + (2-x)C$  (Eq. (33)), (d)  $O_2 + 2V_O \rightarrow 2O_O$  (Eq. (34)), without mixing entropy, and (e) same as (d) but considering mixing entropy. (a)-(d) refer to legend.  $UC_{2-x}$  can decompose into  $U_2C_3$  below 1787 K, however, the decomposition reaction has very slow kinetics and, consequently, it is not considered here. The thermodynamic functions for U, C,  $O_2$ , and CO are taken from [40]. The standard state enthalpies for U, C,  $O_2$  are zero.

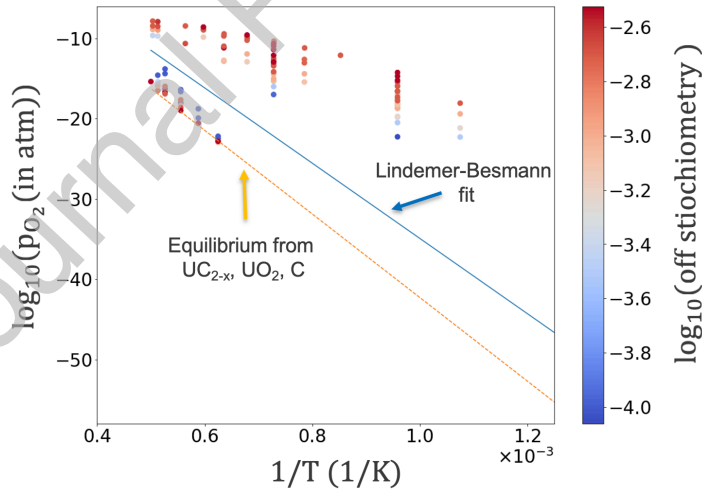


Figure 4: The partial pressure of  $O_2$  as a function of inverse temperature. The solid line is the Lindemer-Besmann model fit [60] for stoichiometric  $UO_2$ . The dashed line is the equilibrium line from  $UC_{2-x}$ ,  $UO_2$ , and C (Eq. (33)). The scattered symbols are experimental data of  $UO_{2\pm x}$  from [60–68] and the color corresponds to  $x$ .

version with a random mixing entropy included (assuming 1% oxygen vacancies), and another version not considering mixing entropy. For the line that

considers the mixing entropy, at high temperatures the reaction in Eq. (34) is less stable than that in Eq. (33), which is the controlling chemical reaction

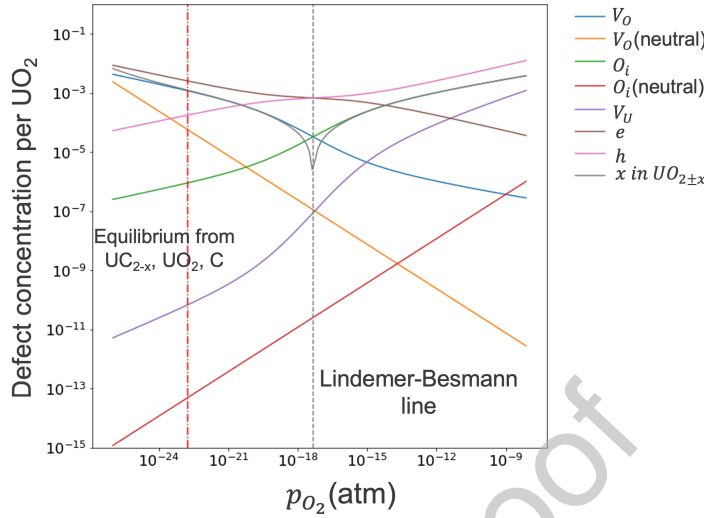


Figure 5: The concentration of defects (per  $\text{UO}_2$  formula unit) as a function of oxygen partial pressure calculated at 1600 K. The solid black line with symbol “x” is the calculated “x” in the non-stoichiometric  $\text{UO}_{2\pm x}$ . The vertical dashed grey line is Lindemer-Besmann model [60] for stoichiometric  $\text{UO}_2$ . The vertical dashed red line is the equilibrium from  $\text{UC}_{2-x}$ ,  $\text{UO}_2$ , and C in the UCO thermal equilibrium Eq. (33).

that determines the UCO thermal equilibrium in the fuel kernel. Or vice versa, it is expected that a high oxygen vacancy concentration will exist in the  $\text{UO}_2$  phase of UCO fuel kernels. In the Ellingham diagram plotted in Fig. 3, only Eq. (34) uses data from DFT+ $U$  calculations. All other lines use thermodynamic functions derived from experiments.

As further validation of the above conclusion, it is possible to directly compare the UCO oxygen partial pressures to experimental data of  $\text{UO}_2$  non-stoichiometry as function of partial pressure. Lindemer and Besmann [60] surveyed past experimental measurements of non-stoichiometric  $\text{UO}_2$  and fitted an exactly stoichiometric  $\text{UO}_2$  line describing the partial pressure of  $\text{O}_2$  as a function of inverse temperature ( $1/T$ ) for the stoichiometric composition. In Fig. 4, the equilibrium  $\text{O}_2$  partial pressure from Eq. (33), which is the controlling chemical reaction that determines the UCO thermal equilibrium in the fuel kernel, along with the Lindemer-Besmann model [60], as well as the experimental data points used in the Lindemer-Besmann analysis [60–68], are shown as a function of  $1/T$ . Obviously, the equilibrium partial pressure of  $\text{UC}_{2-x}$ ,  $\text{UO}_2$ , and C in the fuel kernel points to a strongly reduced (hypostoichiometric)  $\text{UO}_2$  phase.

### 3.4. Defect model and non-stoichiometry predictions

To compute the point defect concentrations at thermal equilibrium conditions in  $\text{UO}_2$ , the defect model defined in Section 2.3 is used. The O/U ratio predicted by the defect model for a given oxygen partial pressure at a specific temperature is governed by the underlying oxygen point defect energies calculated from DFT and the entropies calculated from empirical potentials. There are a number of known inaccuracies in the atomic scale data that could lead to a different O/U ratio for a given oxygen partial pressure than those found in experiments. One known issue is the band gap of  $\text{UO}_2$ , which has been measured to be 2.1 eV [33], however, the energy of the electron-hole reaction Eq. (37), is 1.36 eV from DFT+ $U$ ,



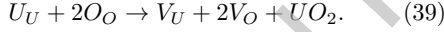
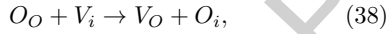
As a result, the oxygen partial pressure for stoichiometric  $\text{UO}_2$  predicted from the defect model is not able to match the Lindemer-Besmann model [60], which was derived by fitting to experimental data.

To match the Lindemer-Besmann model [60], the DFT computed values are modified in a way that the essential defect formation energies are minimally changed. The defect formation energies (e.g.,

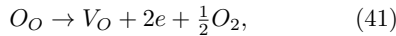
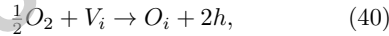
Table 3: The modification of DFT enthalpy and entropy values to match the Lindemer-Besmann model [60]. The enthalpies ( $H$ ,  $\Delta H$ ) are in eV while the entropies ( $S$ ,  $\Delta S$ ) are in  $k_B$  [32], and all values, except those of the  $O_2$  molecule, are relative to their corresponding perfect  $UO_2$  bulk values. For entropies, the values computed at 900 K are used. The temperature dependence for the defects entropy will cancel exactly for all reactions considered in this work. The enthalpies (entropies) are based on calculations using  $3 \times 3 \times 3$  ( $5 \times 5 \times 5$ )  $UO_2$  unit cells, or 108 (500)  $UO_2$  formula units. All enthalpies are evaluated at 0 K.

Defects	modified $H$	original $H$	change in $H$	modified $S$	original $S$	change in $S$
$e$	10.76(1)	10.14(5)	0.62	6.33	6.69	-0.36
$h$	-8.65	-8.79	0.14	-5.60	-5.96	0.36
$V_U$	53.55	54.23	-0.68	12.30	11.21	1.09
$V_O$	-7.65	-7.99	0.34	-10.07	-9.53	-0.55
$O_i$	11.38	11.82	-0.44	15.77	15.23	0.55
$O_2$ molecule	-10.48	-10.48	0.0	28.87	28.87	0.0
Reactions	modified $\Delta H$	original $\Delta H$	change in $\Delta H$	modified $\Delta S$	original $\Delta S$	change in $\Delta S$
Electron-hole pair (Eq. (37))	2.11	1.36	0.75	0.73	0.73	0.0
Oxygen Frenkel pair (Eq. (38))	3.73	3.83	-0.10	5.70	5.70	0.0
Schottky trio (Eq. (39))	6.45	6.45	0.0	8.49	8.49	0.0
Oxidation per oxygen (Eq. (40))	-0.68	-0.51	-0.17	-9.87	-11.13	1.26
Reduction per oxygen (Eq. (41))	8.63	7.07	1.56	17.03	18.29	-1.26

for an oxygen interstitial) are allowed to change, it is just the stoichiometric reactions below (Eq. (38) and Eq. (39)) that are minimally changed. The essential defect formation energies include the oxygen Frenkel pair formation energy, as shown in Eq. (38), and Schottky formation energy, as shown in Eq. (39) below,



In Eq. (38),  $O_i$  is the oxygen interstitial.  $V_U$  is the uranium vacancy in Eq. (39). The modifications of the DFT and empirical potential values and the resulting changes to the oxygen Frenkel pair formation energy (Eq. (38)), Schottky formation energy (Eq. (39)), electron-hole pair formation energy (Eq. (37)), as well as to the oxidation (Eq. (40)) and oxygen reduction (Eq. (41)) energetics as shown below,



are summarized in Table 3. The same modifications have already been applied in our recent study of doped  $UO_2$  [41].

The predicted point defect concentrations obtained from simulations with the energies and entropies modified to match the experimental thermochemistry are shown in Fig. 5, which specifically highlights the concentration of different point defects as a function oxygen partial pressure at 1600

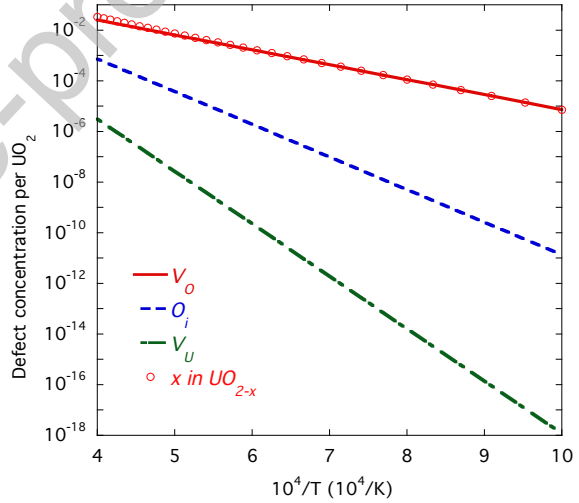


Figure 6: The concentrations of oxygen vacancies, oxygen interstitials, and uranium vacancies (per  $UO_2$  formula unit) in  $UO_{2-x}$  in UCO fuel kernel at different temperatures. The calculated “ $x$ ” in  $UO_{2-x}$  is also shown.

K. As expected, the predicted oxygen partial pressure for stoichiometric  $UO_2$  matches the Lindemer-Besmann model [60] (dashed grey line). In Fig. 5, it is also shown that the oxygen vacancy concentration corresponding to the equilibrium among  $UC_{2-x}$ ,  $UO_{2-x}$ , and C in the UCO fuel kernels (dashed red line), as defined by Eq. (33), is significant.

Finally, the concentrations of oxygen vacancies, oxygen interstitials, and uranium vacancies in

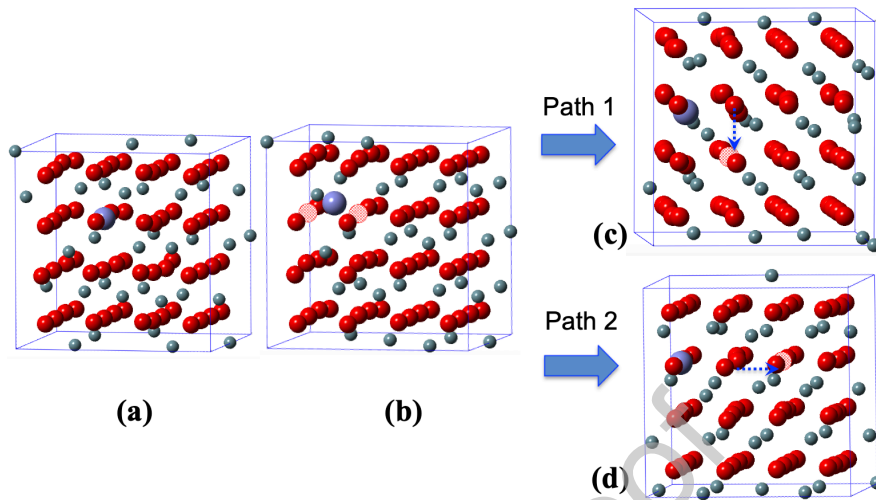


Figure 7: Xe migration mechanisms via oxygen vacancies. (a) A Xe atom occupying an oxygen vacancy site ( $Xe_O$ ). (b) An additional oxygen vacancy migrates to  $Xe_O$  from the left side. (c) Xe migration mechanism by path 1: one oxygen vacancy migrating away from the Xe trap site in the perpendicular direction relative to the direction of the other oxygen vacancy - Xe atom complex. (d) Xe migration mechanism by path 2: one oxygen vacancy migrating away from the Xe trap site in the opposite direction relative to the direction of the other oxygen vacancy - Xe atom complex. Large blue spheres are Xe atoms. Solid red spheres are oxygen atoms. The hatch pattern red sphere is an oxygen vacancy. Small grey spheres are uranium atoms.

$UO_{2-x}$  in UCO fuel kernels at different temperatures are plotted in Fig. 6. The concentration of oxygen vacancies is shown to be consistently many orders of magnitude higher than the concentration of uranium vacancies and oxygen interstitials, which is significantly different from the picture in nearly stoichiometric  $UO_2$ .

#### 4. Xe migration mechanisms in UCO

Under reducing conditions in UCO fuel kernels, diffusion of the fission gas Xe in  $UO_2$  is expected to occur via an interstitial mechanism, an oxygen vacancy mechanism, or via uranium vacancy clusters that dominate for nearly stoichiometric and hyperstoichiometric  $UO_2$ . The oxygen vacancy mechanism was not investigated carefully in previous studies, because it was not expected to be important in LWR  $UO_2$  fuel. Consequently, the thermodynamic and kinetic properties of point defects related to the oxygen vacancy mechanisms must be determined following the same methodology as previously used for  $UO_2$  fuel under LWR conditions (in order to ensure self-consistency) [13].

First, the energy of Xe incorporation into different possible lattice sites in  $UO_{2-x}$  is calculated. The Xe incorporation energy is the energy required

to incorporate an Xe atom in the gas state into a pre-existing defect site in the bulk oxide. An energy of 9.19 eV is required for Xe to occupy the octahedral interstitial site in  $UO_2$ , while the energy for Xe to be incorporated into an existing oxygen vacancy site is 7.48 eV. Obviously, both energies are high, with the oxygen vacancy being slightly lower. For stoichiometric  $UO_2$ , the overall concentration of Xe in oxygen vacancy sites would be smaller than in interstitial sites. This is because the concentration of available oxygen vacancy sites is controlled by the oxygen Frenkel pair formation energy. Such term must be added to the incorporation energy to obtain the solution energy, determining the site preference. However, under reducing conditions the vacancy formation energy is lowered and the concentration goes up, which decreases the solution energy of Xe in oxygen vacancy sites. It is expected that the concentration of Xe in oxygen vacancy sites is comparable to Xe interstitials in  $UO_{2-x}$ . Centipede automatically takes care of this by solving the site distributions.

Next, the Xe interstitial migration energetics is investigated. There are three possible migration mechanisms for Xe diffusion by interstitials: (1) direct hopping, (2) asymmetric hopping [36], and (3) interstitialcy [69]. In asymmetric hopping, the Xe

Table 4: The migration energy for Xe diffusion by various Xe interstitial mechanisms.

	Regular DFT	DFT + $U$
Interstitialcy	1.6 eV [69]	1.0 eV <sup>a</sup> , -0.3 eV [70]
Asymmetric hopping	-	2.1 eV <sup>a</sup> , 0.6 eV [70]
Direct hopping	4.5 – 5.3 eV [71, 72]	5.5 eV [70]

<sup>a</sup> This work.

interstitial pushes a neighboring oxygen atom out of its lattice site, away from one of the neighboring U atoms in the migration process. In Table 4, the migration barriers for Xe diffusion by various Xe interstitial mechanisms are reported. The direct hopping energy is rather high for Xe interstitials, more than 4.5 eV from DFT, as previously reported [71, 72], which was also confirmed in a more recent DFT+ $U$  study [70]. In our work, we find that the lowest-energy migration barrier for Xe interstitial diffusion is by the interstitialcy mechanism, confirming the earlier calculation based on regular DFT [69], with a notably lower migration energy of 1.0 eV compared to the earlier report of 1.6 eV [69]. The second lowest migration energy occurs via asymmetric hopping of Xe interstitials, 2.1 eV. The asymmetric hopping mechanism was identified during the study of a helium interstitial migration in UO<sub>2</sub> [36], which was found to be the lowest migration event in that case. Comparing to a more recent DFT+ $U$  study [70], although the trend in the Xe interstitial migration mechanisms is similar, the actual values are quite different. The reason for this difference is not yet understood. One possible source of the discrepancy could be due to rigidly applying the on-site orbital occupation matrix of bulk UO<sub>2</sub> as a starting point for defect calculations in the previous work [70]. In our experience, when the lattice distortions surrounding the defect are large, such as in the Xe interstitial case, this approach often results in a higher (metastable) energy state.

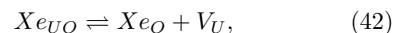
Following the interstitial migration mechanisms, Xe diffusion by oxygen vacancies is explored. The mechanism investigated involves Xe in an oxygen vacancy site diffusing by the binding a second oxygen vacancy (XeO<sub>2</sub>). In Fig. 7(a), a Xe atom in an oxygen vacancy site is shown and in Fig. 7(b), an additional oxygen vacancy migrates to Xe<sub>O</sub> from the left side. Xe is found to be located approximately mid-way between the two bound oxygen vacancies, which results in a binding energy of -0.3 eV, where the negative sign corresponds to at-

traction. For Xe diffusion via an oxygen vacancy mechanism, we consider two cases. Case 1 is an oxygen vacancy migrating away from the Xe trap site in the direction perpendicular to the original Xe trap site (as shown in Fig. 7(c)). The other case (case 2) is for an oxygen vacancy migrating away from the Xe trap site in the opposite direction (as shown in Fig. 7(d)). In both cases, the Xe atom will have a net displacement starting from its original position occupying an oxygen vacancy. In case 1, the migration energy is 0.92 eV, while the migration energy in case 2 is 0.69 eV. In case 2, the final configuration is 0.46 eV higher than the starting configuration. In the absence of Xe, the oxygen vacancy migration barrier was calculated to be 0.67 eV by Dorado et al. using DFT+ $U$  [73]. This is almost same as the 0.69 eV migration energy barrier for the case 2 mechanism. Based on these DFT+ $U$  results, the effective migration energy for Xe diffusion by oxygen vacancies is set to 0.69 eV. The migration frequencies for both migration mechanisms (by Xe interstitial and by the oxygen vacancy) were assumed to be 10<sup>12</sup> Hz.

Table 5: Xe migration and binding energies from DFT+ $U$ .

	Binding energy (eV)	Binding entropy (k <sub>B</sub> )	Migration energy (eV)
Xe <sub>i</sub>	9.19	3.76	1.0
Xe <sub>O</sub>	7.48	-0.76	-
XeO <sub>2</sub>	6.49	-0.2359	0.69

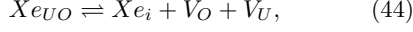
In order to include Xe diffusion by interstitials and oxygen vacancies in the Centipede cluster dynamics model previously developed for UO<sub>2</sub> in LWR applications [13], the thermodynamic defect properties (binding energies) must be calculated in addition to the migration properties. The binding energies are used for determination of the defect concentrations under thermal equilibrium, which is also important for the calculation of driving forces under irradiation. The binding energies are all relative to the Xe<sub>VO</sub> cluster, which is defined as the zero energy reference state [13], although neither the results nor the conclusions are sensitive to the choice of reference. For example, in the case of Xe<sub>O</sub>, the chemical reaction



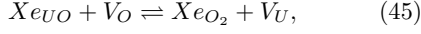
defines the binding energy of Xe<sub>O</sub>. This means that the binding energy can be calculated as,

$$E_b(Xe_O) = E_b(Xe_{VO}) + E_{Xe_O} + E_{V_U} - E_{Xe_{VO}}. \quad (43)$$

This is done similarly for  $Xe_i$  and  $Xe_{O_2}$ . The reactions are,



and,



respectively<sup>3</sup>. The binding entropies are calculated in a similar way using results from empirical potential calculations. Table 5 lists the values calculated from DFT. The DFT and empirical potential energy and entropy values are used as inputs to the Centipede cluster dynamics simulations (see Section 6), together with the data for Xe occupying uranium and oxygen vacancy clusters in  $UO_2$  [13]. In thermal equilibrium, the concentration of a defect cluster  $Xe_{U_xO_y}$  can be computed by the following formula,

$$\frac{[Xe_{U_xO_y}]}{[Xe_{UO}]} = C_{U_xO_y} [V_U]^{(x-1)} [V_O]^{(y-1)} e^{-\frac{G_b(Xe_{U_xO_y})}{k_B T}}, \quad (46)$$

where  $C_{U_xO_y}$  is the multiplicity factor,  $[V_U]$  is the uranium vacancy concentration,  $[V_O]$  is the oxygen vacancy concentration, and  $G_b(Xe_{U_xO_y})$  is the Gibbs free energy for the binding energetics of the cluster  $Xe_{U_xO_y}$ . The analytical solution for thermal equilibrium conditions can be used for validation of the Centipede code (in the absence of irradiation), which solves the full set of equations describing the defect evolution under both thermal equilibrium and irradiation.

## 5. Thermal and irradiation-enhanced fission gas diffusion coefficients

The final thermal and irradiation-enhanced Xe diffusion coefficients in UCO fuel kernels are calculated by using the cluster dynamics code Centipede. In order to extend from simulations focused on  $UO_2$  for LWR applications to UCO or  $UO_{2-x}$  fuel kernels, three main changes are made in Centipede to accommodate the new physics. These are: (1) New partial pressure formulation (Eq. (33)), which is key for capturing defect formation energies; (2) Addition of Xe + oxygen vacancy clusters based on the properties calculated from atomistics; and (3) Xe

interstitial sourcing effect – Xe knockout from small clusters into interstitial sites – which represents a reaction that conserves species, for  $Xe_i$  behavior.

By using the approximation that oxygen defects are so fast that they maintain thermal equilibrium under irradiation at all temperatures of interest [15], the relative concentrations of defects that differ by the oxygen vacancy or interstitial coordination can be trivially calculated. For example,

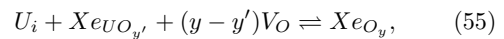
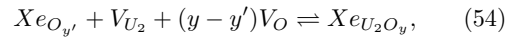
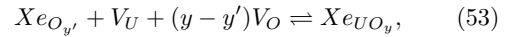
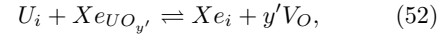
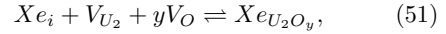
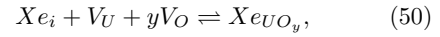
$$[Xe_{U_4O_3}] = [Xe_{U_4O_4}] \frac{[Xe_{U_4O_3}]_{th}}{[Xe_{U_3O_4}]_{th}}. \quad (47)$$

Similarly, Xe in an oxygen vacancy can be treated much the same way with respect to the Xe interstitial,

$$[Xe_{eO}] = [Xe_i] \frac{[Xe_{eO}]_{th}}{[Xe_i]_{th}}, \quad (48)$$

$$[Xe_{eO_2}] = [Xe_i] \frac{[Xe_{eO_2}]_{th}}{[Xe_i]_{th}}. \quad (49)$$

This turns  $Xe_{eO}$  and  $Xe_{eO_2}$  into linked clusters, in that their concentrations can be analytically calculated given the concentration of  $Xe_i$ , and vice versa. The code internals do not explicitly solve each of these reactions, but rather propagate the concentration loss across all linked clusters:



, where  $y'$  and  $y$  indicate the range of oxygen vacancies bound to each cluster on the left- and right-hand side of the equations, respectively. The corresponding oxygen vacancies are added to the equations for species conservation. The linkage occurs through these oxygen vacancies, which, as previously mentioned, are assumed to be in thermal equilibrium due to the rapid diffusion of oxygen defects.

As shown in Fig. 8, at thermal equilibrium conditions, Xe diffusion in the UCO fuel kernel is primarily through  $Xe_{eO_2}$  at low temperatures, and through  $Xe_{U_2O}$  at high temperatures, with the transition between the two mechanisms occurring at around 1750 K. This is fundamentally different from the  $UO_2$  case in the absence of irradiation where Xe

<sup>3</sup>For  $Xe_i$  and  $Xe_{eO}$ , the binding energies as defined by Eqs. (44) and (45) respectively, have the same values as the values of the Xe incorporation energies.

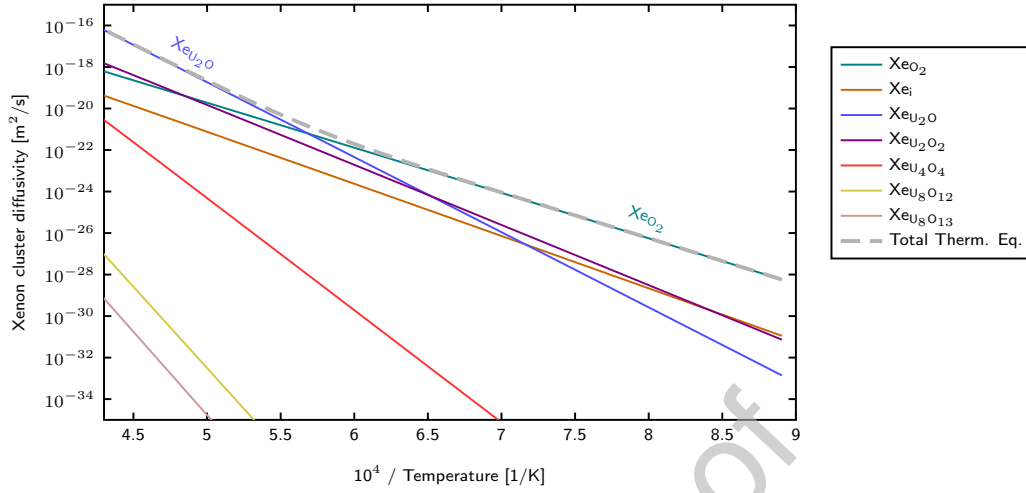


Figure 8: Xe diffusivity contributions for  $\text{UO}_2$  in UCO fuels from different defect clusters under thermal equilibrium as a function of inverse temperature. The total Xe diffusivity under thermal equilibrium is also given (the grey dashed line).

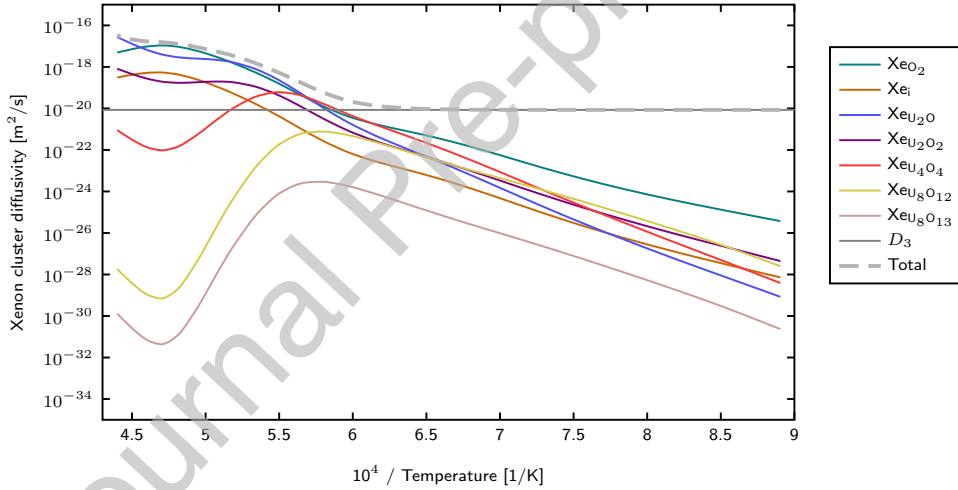


Figure 9: Xe diffusivity contributions from different defect clusters under irradiation as a function of inverse temperature. The total Xe diffusivity under irradiation, including the athermal diffusivity,  $D_3$ , is also given (the grey colored solid line). The simulations are run with a fission rate density  $f'''$  of  $1 \times 10^{19}$  fission/ $\text{m}^3\text{s}$ , and the oxygen partial pressure fixed by the equilibrium from  $\text{UO}_2$ ,  $\text{UC}_{2-x}$ , and C.

diffusion is mainly through  $\text{Xe}_{\text{U}_2\text{O}}$  at all temperatures considered.

The main contribution of the Centipede simulations is not diffusion under thermal equilibrium conditions, but rather to estimate the fission gas diffusivity in UCO fuel kernels under irradiation. In Fig. 9, the Xe diffusivity under irradiation as a function of inverse temperature is shown for a standard fission rate of  $1 \times 10^{19}$  fissions per  $\text{m}^3$  per second,

and  $10^4$  uranium Frenkel pairs generated per fission. At temperatures up to 2000 K, diffusion is primarily through  $\text{Xe}_{\text{O}_2}$ , while at very high temperatures diffusion primarily occurs via the same  $\text{Xe}_{\text{U}_2\text{O}}$  mechanism as under thermal equilibrium conditions. The transition temperature is at  $\sim 2200$  K. Again, this is very different from standard LWR  $\text{UO}_2$  fuels, where at low temperatures the  $\text{Xe}_{\text{U}_4\text{O}_3}$  cluster dominates, and at high temperatures diffusion occurs due to

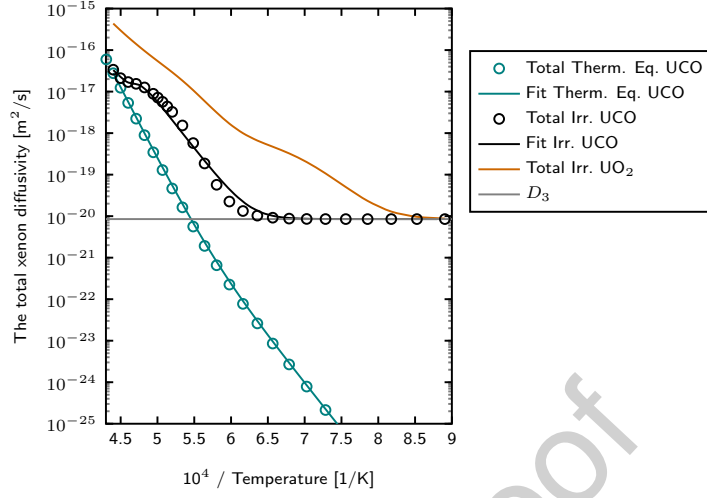


Figure 10: The total Xe diffusivity in UCO under thermal equilibrium ( $D_1$  term, turquoise circles) and total Xe diffusivity under irradiation (the sum of  $D_1 + D_2 + D_3$ , black circles). The light grey solid line is the fission rate density dependent athermal diffusivity,  $D_3$ . The total Xe diffusion coefficient in LWR  $\text{UO}_2$  is also plotted (orange solid line). The turquoise solid line is the fitted result of  $D_1$  and the black solid line is the fitted result of  $D_1 + D_2 + D_3$  under irradiation.

the  $\text{Xe}_{\text{U}_2\text{O}}$  cluster. Essentially, larger clusters are suppressed in the UCO case compared to the standard LWR conditions. This is mainly due to the oxygen partial pressure change in the UCO case. It is clear from the Centipede simulations that both  $\text{Xe}_\text{O}$  and  $\text{Xe}_{\text{O}_2}$  are important for UCO. It is also confirmed that  $\text{Xe}_i$  sourcing does not have any major impact on the overall behavior.

Similar to past treatments of  $\text{UO}_2$  for LWR applications, the diffusivity over the entire temperature range can be split into a temperature dependent intrinsic high temperature diffusivity,  $D_1$ , a fission rate density dependent athermal diffusivity  $D_3$ , and a complex intermediate term dependent on temperature and fission rate density,  $D_2$ . The total Xe diffusivities in UCO under thermal equilibrium and irradiated conditions are plotted in Fig. 10. The  $D_3$  term is assumed to be the same for both the UCO and  $\text{UO}_2$  cases. It is clear that diffusion is much slower in UCO than in  $\text{UO}_2$  and the  $D_2$  transition occurs at much higher temperatures.

Finally, in order to provide an input that can easily be used in the Bison fuel performance code, the Centipede simulation results are fitted to exponential functions. For the  $D_1$  term, which represents Xe diffusion under thermal equilibrium, an equation with two exponential terms is adequate to describe the simulation data. The results for the  $D_2$  term (radiation-enhanced diffusion) is more com-

plicated. The fitted equations are also plotted in Fig. 10. The fitted equations for the  $D_1$  and  $D_2$  terms are,

$$D_1 = 5.2122 \times 10^{-2} \exp\left(-\frac{79948}{T}\right) + 3.4834 \times 10^{-9} \exp\left(-\frac{51197}{T}\right) (\text{m}^2/\text{s}), \quad (56)$$

$$D_2 = \frac{1 \times 10^{-6} \exp\left(-\frac{51800}{T}\right)}{1 + 3.77 \times 10^{21} \exp\left(-\frac{105600}{T}\right)} (\text{m}^2/\text{s}) \quad (57)$$

The above simulations are run with a fission rate density  $f'''$  of  $10^{19}$  fission/ $\text{m}^3\text{s}$ . It has been shown earlier that  $D_2$  term has a square root dependence on the fission rate density while  $D_3$  term scales linearly with the fission rate density. After considering these relationships, the diffusion terms now become,

$$D_2 = \frac{3.1623 \times 10^{-16} \exp\left(-\frac{51800}{T}\right)}{1 + 3.77 \times 10^{21} \exp\left(-\frac{105600}{T}\right)} \sqrt{f'''} (\text{m}^2/\text{s}) \quad (58)$$

$$D_3 = 8.5 \times 10^{-40} f''' (\text{m}^2/\text{s}) \quad (59)$$

## 6. Implementation and testing of UCO diffusion model in Bison

The diffusion coefficients of  $\text{UO}_2$  in UCO kernels are tested for a TRISO fuel particle under the representative irradiation conditions given in Table 6.

Table 6: Irradiation conditions for Bison fuel performance simulations of a TRISO particle.

Conditions	Effective Full Power Day (EFPD)	Burnup (%FIMA)	Fast fluence ( $\times 10^{25}$ n/m <sup>2</sup> ), $E > 0.18$ MeV	Irradiation temperature (K)
1	510	14.5	5.11	1200
2	510	14.5	5.11	1450
3	510	14.5	5.11	1700
4	510	14.5	5.11	1950
5	510	14.5	5.11	2100

The fuel parameters given in Table 7 are based on the AGR-5/6/7 fuel specification [74]. The composition of the fuel has uncertainty with regard to whether it lies within (UO<sub>2</sub>, UC<sub>2</sub>, C) or (UO<sub>2</sub>, UC, UC<sub>2</sub>) phase region. However, since the main purpose of the present study is to test the effect of the UCO diffusion model in Bison simulations, we did not attempt to modify the analysis to account for the second phase region listed above. The inclusion of the second phase could impact the detailed modeling result, although we do not expect the general trend to change.

The volume used to compute internal pressure consists of the gap between the buffer and IPyC layer and voids inside the kernel and buffer layer. The voids of the buffer layer is calculated as the ratio of buffer density to its theoretical density.

The FGR (moles), internal pressure and tangential stress of the SiC layer are plotted in Fig. 11, Fig. 12 and Fig. 13, respectively. As seen from all three plots, at temperatures of 1950 K and 2100 K, the difference between the UCO and UO<sub>2</sub> diffusion coefficients is invisible. At temperature above 1950 K, both UCO and UO<sub>2</sub> diffusion coefficients are sufficiently large that the Booth release fraction computed in Eq. (14) is very close to one. At other temperatures, the FGR and pressure obtained for UCO diffusion coefficients are smaller than for the standard UO<sub>2</sub> case, with the largest difference occurring at 1450 K. As a consequence, the compressive tangential stress in the SiC layer becomes higher at higher fluence as less internal pressure is built up by fission gas release. Since a traditional pressure vessel failure of the SiC layer in TRISO particles is expected to occur when sufficient pressure makes the tangential stress of the SiC layer exceed its tensile strength, the pressure vessel failure is less likely to happen for UCO TRISO fuel particles.

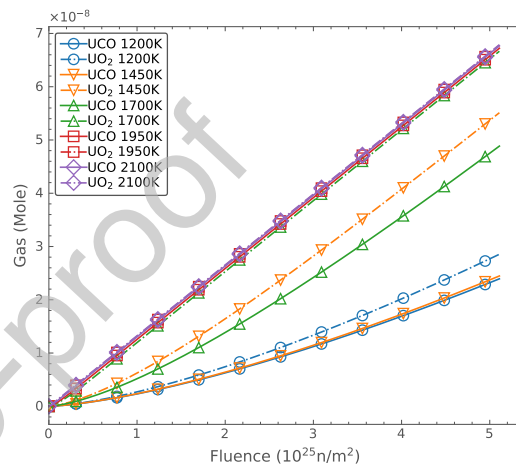


Figure 11: Fission gas release calculated in a Bison fuel performance simulation of a TRISO particle. “UO<sub>2</sub>” cases use diffusion coefficients of UO<sub>2</sub> obtained by [15], while “UCO” cases use diffusion coefficients of UCO obtained by this lower length scale study.

## 7. Conclusions

UCO fuel kernels made from a mixture of UO<sub>2</sub> and uranium carbide prevent formation of CO gas in TRISO fuel particles and are considered to be more accident tolerant than just UO<sub>2</sub> for usage in next generation reactors, including fluoride salt-cooled high temperature reactors and micro-reactors. Given the importance of TRISO fuels for advanced reactor concepts actively pursued by industry, better understanding and more accurate performance models of the TRISO fuel kernels are high priorities. The current state-of-the-art models in fuel performance codes such as PARFUME [6] still use the release data for Xe obtained from light water reactor UO<sub>2</sub> fuel, which is nearly stoichiometric or slightly hyperstoichiometric. However, in actual UCO fuel kernels, the fission gas release rate is expected to be different, because of the more reducing conditions in UCO compared to light water

Table 7: Fuel parameters for Bison fuel performance simulations of a TRISO particle.

Category	Parameter	Nominal values
Fuel characteristics	$^{235}\text{U}$ enrichment (wt%)	15.5
	Carbon/uranium (atomic ratio)	0.4
	Oxygen/uranium (atomic ratio)	1.5
Particle geometry	Kernel diameter( $\mu\text{m}$ )	425
	Buffer thickness( $\mu\text{m}$ )	100
	IPyC/OPyC thickness ( $\mu\text{m}$ )	40
	SiC thickness ( $\mu\text{m}$ )	35
Fuel properties	Kernel density ( $\text{g}/\text{cm}^3$ )	11.0
	Kernel theoretical density( $\text{g}/\text{cm}^3$ )	11.4
	Buffer density( $\text{g}/\text{cm}^3$ )	1.05
	Buffer theoretical density( $\text{g}/\text{cm}^3$ )	2.25
	IPyC density ( $\text{g}/\text{cm}^3$ )	1.90
	OPyC density ( $\text{g}/\text{cm}^3$ )	1.90
	IPyC/OPyC Bacon Anisotropy Factor (BAF)	1.05

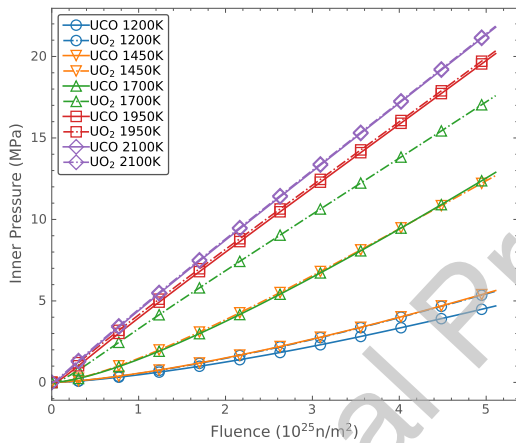


Figure 12: Inner pressure calculated in a Bison fuel performance simulation of a TRISO particle. “UO<sub>2</sub>” cases use diffusion coefficients of UO<sub>2</sub> obtained by [15], while “UCO” cases use diffusion coefficients of UCO obtained by this lower length scale study.

reactor UO<sub>2</sub> fuel.

In this work, based on prior studies of fission gas diffusion in UO<sub>2</sub> for light water reactors under both intrinsic conditions and under irradiation, a lower length scale modeling and simulation study of the fission gas Xe in UCO TRISO fuel kernels have been carried out. The approach relies on density functional theory and empirical potential calculations to determine Xe and point defect properties, which are then used in thermodynamic and kinetic models to predict diffusion for intrinsic conditions, while cluster dynamics simulations are used for the irradiation response.

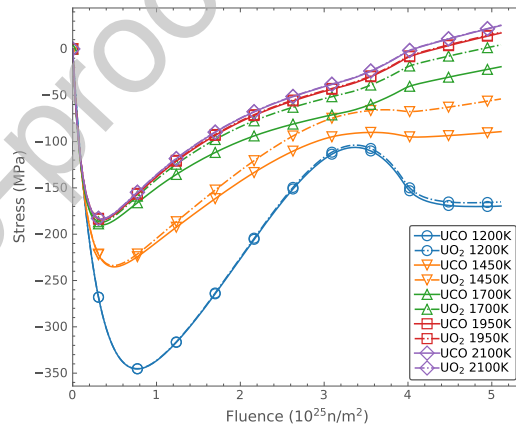


Figure 13: Tangential stress at the inner surface of the SiC layer calculated in a Bison fuel performance simulation of a TRISO particle. “UO<sub>2</sub>” cases use diffusion coefficients of UO<sub>2</sub> obtained by [15], while “UCO” cases use diffusion coefficients of UCO obtained by this lower length scale study.

The high positive heats of mixing from DFT calculations suggest that UO<sub>2</sub> and UC<sub>2</sub> exist as separate phases in UCO fuel kernels, in agreement with experimental observations. The presence of UC<sub>2</sub> (or UC<sub>2-x</sub>) and C in the UCO fuel kernels is shown to have substantial impact on the UO<sub>2</sub> non-stoichiometry by inducing oxygen vacancies and driving UO<sub>2</sub> sub-stoichiometric, which is also consistent with experiments. In particular, the equilibrium oxygen partial pressure of UC<sub>2-x</sub>, UC<sub>2</sub>, and C in the fuel kernel points to a strongly reduced (hypostoichiometric) UO<sub>2</sub> phase. The point defect concentrations at thermal equilibrium conditions are calculated based on a Gibbs free en-

ergy defect model, with the DFT energies and entropies calculated from empirical potentials modified to match the experimental thermo-chemistry. Furthermore, the DFT calculated parameters for Xe diffusion by interstitials and oxygen vacancies are incorporated into the Centipede cluster dynamics code previously developed for  $\text{UO}_2$  in LWR applications. This code solves the full set of equations describing the defect evolution under both thermal equilibrium and irradiation. The resulting diffusion coefficient is lower than in standard LWR  $\text{UO}_2$ .

The new diffusion coefficients from the Centipede simulations are then tested for fission gas retention/release in a TRISO fuel particle under representative irradiation conditions in the fuel performance code Bison. At moderate temperatures between 1200 K and 1700 K, the compressive tangential stress in the SiC layer becomes larger at higher fluence as less internal pressure is built up by fission gas release. This causes pressure vessel failure of the SiC layer to be less likely to occur.

### Acknowledgements

We thank Steven Novascone at Idaho National Laboratory for helpful discussions. This work was funded by the U.S. Department of Energy (DOE), Office of Nuclear Energy, Nuclear Energy Advanced Modeling and Simulation (NEAMS) program. The results presented in this paper were supported in part by the DOE Nuclear Energy University Programs (NEUP) Integrated Research Project 20-22094 “Multi-physics fuel performance modeling of TRISO-bearing fuel in advanced reactor environments”. Los Alamos National Laboratory, an affirmative action/equal opportunity employer, is operated by Triad National Security LLC, for the National Nuclear Security Administration of the U.S. Department of Energy under Contract No. 89233218CNA000001.

### References

- [1] P. Demkowicz, B. Liu, J. Hunn, Coated particle fuel: Historical perspectives and current progress, *J. Nucl. Mater.* 515 (2019) 434–450.
- [2] D. Petti, An overview of the doe advanced gas reactor fuel development and qualification program, in: Presentation given at the Workshop on Advanced Reactors with Innovation Fuels (ARWIF), Oak Ridge, Tennessee, February 16 (2005).
- [3] Online resource (2020). URL <https://www.nrc.gov/reactors/new-reactors/advanced/kairos.html>
- [4] Online resource (2020). URL [https://inldigitallibrary.inl.gov/sites/sti/sti/Sort\\_7262.pdf](https://inldigitallibrary.inl.gov/sites/sti/sti/Sort_7262.pdf)
- [5] J. Powers, B. Wirth, A review of triso fuel performance models, *J. Nucl. Mater.* 405 (2010) 74–82.
- [6] G. Miller, D. Petti, J. Maki, D. Knudson, W. Skerjanc, PARFUME Theory and Model Basis Report, Report INL/EXT-08-14497 (Rev.1), Idaho National Laboratory (September 2018).
- [7] W. Miekeley, F. W. Felix, Effect of stoichiometry on diffusion of xenon in  $\text{UO}_2$ , *J. Nucl. Mater.* 42 (1972) 297–306.
- [8] H. Matzke, Atomic mechanisms of mass transport in ceramic nuclear fuel materials, *J. Chem. Soc., Faraday Trans.* 86 (1990) 1243–1256.
- [9] T. Tiegs, T. Lindemer, T. Henson, Fission product behavior in  $\text{UC}_x\text{O}_y$  fissile particles made from weak-acid resins, *J. Nucl. Mater.* 99 (2) (1981) 222–234.
- [10] R. Bullock, Fission-product release during postirradiation annealing of several types of coated fuel particles, *J. Nucl. Mater.* 125 (3) (1984) 304–319.
- [11] D. Petti, J. Maki, J. Hunn, P. Pappano, C. Barnes, J. Saurwein, S. Nagley, J. Kendall, R. Hobbins, The DOE advanced gas reactor fuel development and qualification program, *JOM* 62 (9) (2010) 62–66.
- [12] D. A. Andersson, P. Garcia, X.-Y. Liu, G. Pastore, M. Tonks, P. Millett, B. Dorado, D. R. Gaston, D. Andrs, R. L. Williamson, R. C. Martineau, B. P. Uberuaga, C. R. Stanek, Atomistic modeling of intrinsic and radiation-enhanced fission gas (Xe) diffusion in  $\text{UO}_{2\pm x}$ : Implications for nuclear fuel performance modeling, *J. Nucl. Mater.* 451 (2014) 225–242.
- [13] R. Perriot, C. Matthews, M. Cooper, B. Uberuaga, C. Stanek, D. Andersson, Atomistic modeling of out-of-pile xenon diffusion by vacancy clusters in  $\text{UO}_2$ , *J. Nucl. Mater.* 520 (2019) 96–109.
- [14] C. Matthews, R. Perriot, M. W. Cooper, C. R. Stanek, D. A. Andersson, Cluster dynamics simulation of uranium self-diffusion during irradiation in  $\text{UO}_2$ , *J. Nucl. Mater.* 527 (2019) 151787.
- [15] C. Matthews, R. Perriot, M. M. Cooper, C. R. Stanek, D. A. Andersson, Cluster dynamics simulation of xenon diffusion during irradiation in  $\text{uo}_2$ , *J. Nucl. Mater.* 540 (2020) 152326.
- [16] R. Williamson, J. Hales, S. Novascone, M. Tonks, D. Gaston, C. Permann, D. Andrs, R. Martineau, Multidimensional multiphysics simulation of nuclear fuel behavior, *J. Nucl. Mater.* 423 (1) (2012) 149–163.
- [17] J. Hales, R. Williamson, S. Novascone, D. Perez, B. Spencer, G. Pastore, Multidimensional multiphysics simulation of TRISO particle fuel, *J. Nucl. Mater.* 443 (1) (2013) 531–543.
- [18] W. Jiang, J. D. Hales, B. W. Spencer, B. P. Collin, A. E. Slaughter, S. R. Novascone, A. Toptan, K. A. Gamble, R. Gardner, Triso particle fuel performance and failure analysis with bison, *Journal of Nuclear Materials* 548 (2021) 152795.
- [19] G. Kresse, J. Hafner, *Ab initio* molecular dynamics for open-shell transition metals, *Phys. Rev. B* 48 (1993) 13115–13118.
- [20] G. Kresse, J. Furthmüller, Efficiency of *ab-initio* total energy calculations for metals and semiconductors using a plane-wave basis set, *Comp. Mater. Sci.* 6 (1996) 15–50.
- [21] G. Kresse, J. Furthmüller, Efficient iterative schemes

- for *ab initio* total-energy calculations using a plane-wave basis set, *Phys. Rev. B* 54 (1996) 11169–11186.
- [22] G. Kresse, D. Joubert, From ultrasoft pseudopotentials to the projector augmented-wave method, *Phys. Rev. B* 59 (1999) 1758–1775.
- [23] P. E. Blöchl, Projector augmented-wave method, *Phys. Rev. B* 50 (1994) 17953–17979.
- [24] A. I. Liechtenstein, V. I. Anisimov, J. Zaanen, Density-functional theory and strong interactions: Orbital ordering in mott-hubbard insulators, *Phys. Rev. B* 52 (1995) R5467–R5470.
- [25] S. L. Dudarev, D. N. Manh, A. P. Sutton, Effect of mott-hubbard correlations on the electronic structure and structural stability of uranium dioxide, *Phil. Mag.* 75 (1997) 613–628.
- [26] X.-D. Wen, S. P. Rudin, E. R. Batista, D. L. Clark, G. E. Scuseria, R. L. Martin, Rotational rehybridization and the high temperature phase of  $UO_2$ , *Inorganic Chemistry* 51 (23) (2012) 12650–12659.
- [27] G. Henkelman, B. P. Uberuaga, H. Jonsson, A climbing image nudged elastic band method for finding saddle points and minimum energy paths, *J. Chem. Phys.* 113 (2000) 9901–9904.
- [28] B. Dorado, B. Amadon, M. Freyss, M. Bertolus, Dft + textitU calculations of the ground state and metastable states of uranium dioxide, *Phys. Rev. B* 79 (2009) 235125.
- [29] B. Meredig, A. Thompson, H. A. Hansen, C. Wolverton, A. van de Walle, Method for locating low-energy solutions within DFT +  $U$ , *Phys. Rev. B* 82 (2010) 195128.
- [30] S. Taylor, F. Bruneval, Understanding and correcting the spurious interactions in charged supercells, *Phys. Rev. B* 84 (2011) 075155.
- [31] J.-P. Crocombette, First-principles study with charge effects of the incorporation of iodine in  $UO_2$ , *J. Nucl. Mater.* 429 (2012) 70–77.
- [32] M. W. D. Cooper, C. R. Stanek, D. A. Andersson, The role of dopant charge state on defect chemistry and grain growth of doped  $UO_2$ , *Acta Mater.* 150 (2018) 403–413.
- [33] J. Schoenes, Optical properties and electronic structure of  $UO_2$ , *J. Appl. Phys.* 49 (1978) 1463–1465.
- [34] R. Perriot, X.-Y. Liu, C. R. Stanek, D. A. Andersson, Diffusion of Zr, Ru, Ce, Y, La, Sr and Ba fission products in  $UO_2$ , *J. Nucl. Mater.* 459 (2015) 90–96.
- [35] M. W. D. Cooper, S. T. Murphy, D. Andersson, The defect chemistry of  $UO_{2\pm x}$  from atomistic simulations, *J. Nucl. Mater.* 504 (2018) 251–260.
- [36] X.-Y. Liu, D. Andersson, Revisiting the diffusion mechanism of helium in  $UO_2$ : A DFT+ $U$  study, *J. Nucl. Mater.* 498 (2018) 373–377.
- [37] J. D. Gale, GULP: A computer program for the symmetry-adapted simulation of solids, *J. Chem. Soc.* 93 (1997) 629–637.
- [38] M. W. D. Cooper, M. J. D. Rushton, R. W. Grimes, A many-body potential approach to modelling the thermomechanical properties of actinide oxides, *J. Phys. Condens. Matter.* 26 (2014) 105401.
- [39] S. T. Murphy, N. Hine, Point defects and non-stoichiometry in  $Li_2TiO_3$ , *Chem. Mater.* 26 (2014) 1629–1638.
- [40] Nist chemistry webbook.  
URL <https://webbook.nist.gov/chemistry>
- [41] M. W. Cooper, G. Pastore, Y. Che, C. Matthews, A. Forslund, C. R. Stanek, K. Shirvan, T. Tverberg, K. A. Gamble, B. Mays, D. A. Andersson, Fission gas diffusion and release for cr2o3-doped  $UO_2$ : From the atomic to the engineering scale, *J. Nucl. Mater.* 545 (2021) 152590.
- [42] T. R. Waite, General theory of bimolecular reaction rates in solids and liquids, *J. Chem. Phys.* 28 (1958) 103.
- [43] B. P. Uberuaga, D. Bacorisen, R. Smith, J. A. Ball, R. Grimes, A. F. Voter, K. E. Sickafus, Defect kinetics in spinels: Long-time simulations of  $MgAl_2O_4$ ,  $MgGa_2O_4$ , and  $MgIn_2O_4$ , *Physical Review B* 75 (10) (2007) 104116.
- [44] U. Littmark, J. Ziegler, Handbook of Range Distributions for Energetic Ions in All Elements, Pergamon Press, 1980.
- [45] A. Booth, A method of calculating gas diffusion from  $UO_2$  fuel and its application to the X-2-f loop test, Tech. Rep. AECL-496, Atomic Energy of Canada Ltd. (1957).
- [46] M. V. Speight, A calculation on the migration of fission gas in material exhibiting precipitation and re-solution of gas atoms under irradiation, *Nuclear Science and Engineering* 37 (2) (1969) 180–185.
- [47] F. S. Ham, Theory of diffusion-limited precipitation, *Journal of Physics and Chemistry of Solids* 6 (4) (1958) 335–351.
- [48] R. White, M. Tucker, A new fission-gas release model, *Journal of Nuclear Materials* 118 (1) (1983) 1–38.
- [49] J. Turnbull, R. White, C. Wise, The diffusion coefficient for fission gas atoms in uranium dioxide, in: International Working Group on Water Reactor Performance and Technology, Proceedings of a Technical Committee Meeting Organized by the International Atomic Energy Agency, Preson, 1988, pp. 174–181.
- [50] J. Turnbull, C. Friskney, J. Findlay, F. Johnson, A. Walter, The diffusion coefficients of gaseous and volatile species during the irradiation of uranium dioxide, *J. Nucl. Mater.* 107 (1982) 168–184.
- [51] H. Holleck, H. Kleykamp, Compounds of Uranium with Carbon, *Gmelin Handbook of Inorganic Chemistry*, 8th ed., U-Suppl., no. C12, 1987.
- [52] P. Chevalier, E. Fischer, Thermodynamic modelling of the C-U and B-U binary systems, *J. Nucl. Mater.* 288 (2001) 100–129.
- [53] C. Guéneau, N. Dupin, B. Sundman, C. Martial, J.-C. Dumas, S. Gossé, S. Chatain, F. D. Bruycker, D. Manara, R. J. Konings, Thermodynamic modelling of advanced oxide and carbide nuclear fuels: Description of the u-pu-o-c systems, *J. Nucl. Mater.* 419 (1) (2011) 145–167.
- [54] I. van Rooyen, Z. Fu, Y. Yang, T. Holesinger, M. Bachhav, Microstructure and Fission Product Distribution Examination in the UCO Kernel of TRISO Fuel Particles, Paper HTR 2018-3012, HTR 2018, Warsaw, Poland, 2018.
- [55] W. B. Wilson, High-temperature x-ray diffraction investigation of the uranium-carbon system, *Journal of the American Ceramic Society* 43 (2) (1960) 77–80.
- [56] F. Homan, T. Lindemer, E. Long, T. Tiegs, R. Beatty, Stoichiometric effects on performance of high-temperature gas-cooled reactor fuels from the U-C-O system, *Nucl. Technol.* 35 (1977) 428–441.
- [57] J. Piazza, M. Sinnott, High temperature phase equilibria in the system carbon-oxygen-uranium, *J. Chem. Eng. Data* 7 (1962) 451–457.
- [58] J. Leitnaker, T. Godfrey, Thermodynamic properties of uranium carbides via the UCO system, *J. Chem. Eng.*

- Data 11 (1966) 392–394.
- [59] E. J. Huber, C. E. Holley, E. H. Meierkord, The heats of combustion of thorium and uranium, *Journal of the American Chemical Society* 74 (13) (1952) 3406–3408.
- [60] T. Lindemer, T. Besmann, Chemical thermodynamic representation of  $(\text{UO}_{2\pm x})$ , *Journal of Nuclear Materials* 130 (1985) 473–488.
- [61] T. Markin, V. Wheeler, R. Bones, High temperature thermodynamic data for  $\text{UO}_{2\pm x}$ , *J. Inorg. Nucl. Chem.* 30 (1968) 807–817.
- [62] V. Wheeler, High temperature thermodynamic data for  $\text{UO}_{2-x}$ , *J. Nucl. Mater.* 39 (1971) 315–318.
- [63] V. Wheeler, I. Jones, Thermodynamic and composition changes in  $\text{UO}_{2\pm x}$  ( $x < 0.005$ ) at 1950 K, *J. Nucl. Mater.* 42 (1972) 117–121.
- [64] N. Javed, Thermodynamic study of hypostoichiometric urania, *J. Nucl. Mater.* 43 (1972) 219–224.
- [65] S. Aronson, J. Belle, Nonstoichiometry in uranium dioxide, *J. Chem. Phys.* 29 (1958) 151–158.
- [66] K. Une, M. Oguma, Oxygen potentials of (U, Gd) $\text{O}_{2\pm x}$  solid solutions in the temperature range 1000–1500°C, *J. Nucl. Mater.* 115 (1983) 84–90.
- [67] K. Une, M. Oguma, Thermodynamic properties of nonstoichiometric urania-gadolinia solid solutions in the temperature range 700–1100°C, *J. Nucl. Mater.* 110 (1982) 215–222.
- [68] K. Hagemark, M. Broli, Equilibrium oxygen pressures over the nonstoichiometric uranium oxides  $\text{UO}_{2+x}$  and  $\text{U}_3\text{O}_{8-z}$  at higher temperatures, *J. Inorg. Nucl. Chem.* 28 (1966) 2837–2850.
- [69] X.-Y. Liu, B. P. Uberuaga, D. A. Andersson, C. R. Stanek, K. E. Sickafus, Mechanism for transient migration of xenon in  $\text{UO}_2$ , *Appl. Phys. Lett.* 98 (2011) 151902.
- [70] E. Torres, T. Kaloni, Thermal conductivity and diffusion mechanisms of noble gases in uranium dioxide: A DFT+*U* study, *J. Nucl. Mater.* 521 (2019) 137–145.
- [71] Y. Yun, H. Kim, H. Kim, K. Park, Atomic diffusion mechanism of Xe in  $\text{UO}_2$ , *J. Nucl. Mater.* 378 (1) (2008) 40–44.
- [72] Y. Yun, O. Eriksson, P. M. Oppeneer, H. Kim, K. Park, First-principles theory for helium and xenon diffusion in uranium dioxide, *J. Nucl. Mater.* 385 (2) (2009) 364–367.
- [73] B. Dorado, P. Garcia, G. Carlot, C. Davoisne, M. Fraczkiewicz, B. Pasquet, M. Freyss, C. Valot, G. Baldinozzi, D. Siméone, M. Bertolus, First-principles calculation and experimental study of oxygen diffusion in uranium dioxide, *Phys. Rev. B* 83 (2011) 035126.
- [74] W. Skerjanc, AGR-5/6/7 Irradiation Test Predictions using PARFUME, Report INL/EXT-17-43189 (Rev.0), Idaho National Laboratory (September 2017).

#### CRedit authorship contribution statement

X.-Y. Liu: Conceptualization, Investigation, Writing - original draft, Visualization, Project administration, Writing - review & editing. C. Matthews: Conceptualization, Investigation, Writing - original draft, Visualization, Project administration, Writing - review & editing. W. Jiang: Conceptualization, Investigation, Writing - original draft, Visualization, Project administration, Writing - review & editing. M.W.D. Cooper: Conceptualization, Investigation, Writing - original draft, Visualization, Project administration, Writing - review & editing. J.D. Hales: Project administration, Software, Writing – review. D.A. Andersson: Conceptualization, Project administration, Writing - review & editing, Funding acquisition.

Journal Pre-proof

**Declaration of interests**

The authors declare that they have no known competing financial interests or personal relationships that could have appeared to influence the work reported in this paper.

The authors declare the following financial interests/personal relationships which may be considered as potential competing interests:

Journal Pre-proof